CHEMISTRY

Backside absorbing layer microscopy: Watching graphene chemistry

Stéphane Campidelli,[1]* Refahi Abou Khachfe,[2] Kevin Jaouen,[1] Jean Monteiller,[1] Claude Amra,[3] Myriam Zerrad,[3] Renaud Cornut,[1] Vincent Derycke,[1] Dominique Ausserré[4]*

The rapid rise of two-dimensional nanomaterials implies the development of new versatile, high-resolution visualization and placement techniques. For example, a single graphene layer becomes observable on Si/SiO_2 substrates by reflected light under optical microscopy because of interference effects when the thickness of silicon oxide is optimized. However, differentiating monolayers from bilayers remains challenging, and advanced techniques, such as Raman mapping, atomic force microscopy (AFM), or scanning electron microscopy (SEM) are more suitable to observe graphene monolayers. The first two techniques are slow, and the third is operated in vacuum; hence, in all cases, real-time experiments including notably chemical modifications are not accessible. The development of optical microscopy techniques that combine the speed, large area, and high contrast of SEM with the topological information of AFM is therefore highly desirable. We introduce a new widefield optical microscopy technique based on the use of previously unknown antireflection and absorbing (ARA) layers that yield ultrahigh contrast reflection imaging of monolayers. The BALM (backside absorbing layer microscopy) technique can achieve the subnanometer-scale vertical resolution, large area, and real-time imaging. Moreover, the inverted optical microscope geometry allows its easy implementation and combination with other techniques. We notably demonstrate the potentiality of BALM by in operando imaging chemical modifications of graphene oxide. The technique can be applied to the deposition, observation, and modification of any nanometer-thick materials.

INTRODUCTION

Graphene and other two-dimensional (2D) materials offer a wide variety of potential applications ranging from low-consumption electronics/optoelectronics and spintronics (*1*–*6*) to materials for energy and catalysis (*7*–*11*) or biological applications (*12*–*15*). The rapid development of these materials sheds light on the importance of the visualization techniques, such as electron microscopies, scanning probe techniques, or Raman mapping. Early on, it was demonstrated that graphene could be observed on Si/SiO_2 by optical microscopy for particular thicknesses of SiO_2 (*16*, *17*). This effect is due to antireflection (AR) interference properties created by the substrate. In the simplest case, the AR property of a coated surface is based on the destructive interference between the light reflected by the two surfaces of a properly chosen layer (nature and thickness).

Graphene oxide (GO) is the oxidized form of graphene produced by the oxidation and exfoliation of graphite. Whereas a single layer of graphene absorbs 2.3% of the incident light (*18*), a monolayer of GO exhibits a much weaker light absorption that makes it almost impossible to distinguish on Si/SiO_2. A few years ago, Jung and co-workers optimized the AR properties of a substrate by depositing silicon nitride layers from 61 to 72 nm on silicon. They were able to directly observe the GO flakes using confocal microscopy at different excitation wavelengths and obtain higher contrast than for graphene on Si/SiO_2 (*19*).

Besides conventional AR layers made of transparent materials (*19*, *20*), AR coatings (ARCs) incorporating absorbing materials (called absorbing ARCs) were introduced when AR properties and light absorption or attenuation were needed (*21*–*23*). These coatings can be either settled on opaque reflective substrates or made of multilayer stacks of absorbing materials and transparent AR layers, and, in all cases, they are used in the "frontside" configuration (that is, the coated surface facing the observer with the light going from the low-index to the high index media—for example, air to glass) (*21*, *24*–*28*). However, absorbing ARCs exhibit an asymmetric behavior: They do not have the same reflectivity depending on which side they are lighted. ARCs made of single layers of absorbing materials [AR and absorbing (ARA) layers] deposited on transparent surface were completely ignored because AR conditions cannot be reached with these materials when they are used in frontside configuration as conventional AR layers. As we demonstrate in the Supplementary Materials, AR conditions can be reached only when the absorbing materials are lighted from the higher index medium. In their application to contrast enhancement, this constraint corresponds to the inverted geometry of a microscope, with the ARA layer deposited on the backside (with respect to the incident light) of a transparent window (*29*). A decisive advantage of this geometry is that the half-space opposite to the microscope, as delimited by the ARA window, is totally empty, hence free for manipulating and probing the sample. Another key asset of using an ARA layer is that it can be conductive, semiconducting, or insulating, which opens the route to new possibilities for direct imaging of electrical, electro-optical, electrochemical, or photochemical phenomena.

Here, we report on the discovery of a new family of single AR layers made of highly absorbing materials and their use as contrast layer in a widefield microscopy technique. We named this technique the backside absorbing layer microscopy (BALM) (see schematic representation in Fig. 1A). We demonstrate that this technique allows imaging of 2D materials, such as GO and MoS_2 easily, both in air and water, and with extremely high resolution. In addition, it also provides chemical contrast. Notably, we are able to clearly differentiate the GO flakes from the reduced GO (r-GO) flakes, even though they only differ by the density of oxygen functions. Conversely to atomic force microscopy (AFM) or scanning electron microscopy (SEM) techniques, it permits monitoring of surface reactions in situ. As examples, we followed the deposition of

[1]Laboratoire d'Innovation en Chimie des Surfaces et Nanosciences (LICSEN), Nanosciences et Innovation pour les Matériaux, la Biomédecine et l'Énergie, CEA, CNRS, Université Paris-Saclay, CEA Saclay, 91191 Gif-sur-Yvette cedex, France. [2]Institut Universitaire de Technologie de Saida, Université Libanaise, Saida, Lebanon. [3]Aix-Marseille Université, CNRS, Centrale Marseille, Institut Fresnel, F-13013 Marseille, France. [4]Institut des Molécules et Matériaux du Mans (UMR 6283), Equipe "Paysages Moléculaires, Horizons Biophotoniques," Université du Maine, Avenue Olivier Messiaen, F-72000 Le Mans, France.
*Corresponding author. Email: stephane.campidelli@cea.fr (S.C.); dominique.ausserre@univ-lemans.fr (D.A.)

nanoparticles on r-GO and took advantage of the high-resolution and real-time imaging of BALM to study the dynamics of the adsorption of small molecules on GO. Finally, we show that, because of its favorable geometry, the BALM technique can be naturally combined with other techniques (particularly electrochemistry) and that its use is not limited to 2D materials.

RESULTS

When made of strongly absorbing materials, the ARA layers are formally defined by the two equations (see the Supplementary Materials for the complete demonstration)

$$n_1^2 - k_1^2 = n_0 n_3 \quad (1)$$

$$e_1 \cong \frac{\lambda}{4\pi} \frac{(n_0 - n_3)}{n_1 k_1} \quad (2)$$

where $n_1 - jk_1$ is the complex refractive index of the ARA layer, e_1 is its thickness, n_0 and n_3 are the refractive indices of the incident and emergent materials, respectively, and λ is the wavelength of light.

These equations correspond to perfect background extinction, and hence maximum contrast for any material trace added on their (back) surface. Using such layers, picometer sensitivity could be attained. However, in practice, the chemical nature of the layer material is often constrained, and the index condition can only be approached, at best, by playing on the working wavelength λ. This is the case with the ARA layers used in this study, which are gold layers with a thickness e_1 of 5 nm. We call these layers near-ARA layers. Note that optimal values of e_1 from Eq. 2 are ca. 3.1 nm in water and 8.7 nm in air [with $n_0 = 1.514$ (glass), $n_3 = 1.334$ (water) or 1.000 (air), $n_1 - jk_1 = 1.3 - 1.8j$ (gold), and $\lambda = 470$ nm]. Although such contrast layers can be further improved, the 5-nm-thick near-ARA layers already appear as a very good compromise for graphene and GO imaging in both air and water.

Figure 1A gives a schematic representation of BALM; the objects under study (GO or other materials) represented by the black square are deposited directly on the near-ARA layer (yellow layer) and lighted from the back. Figure 1B shows the representation of the three configurations exhibiting AR properties: (case i) a conventional AR layer (quarter-wave layer); (case ii) a weakly absorbing AR layer lighted from air; and (case iii) a near-ARA layer lighted from glass, which is the high index medium. BALM corresponds to the latter configuration. Figure 1 (C to F) displays several examples of optical images obtained for GO monolayers deposited from water/SDBS (sodium dodecylbenzene sulfonate) solution (*30*) or chemical vapor deposition–grown MoS_2 monolayers transferred on the near-ARA window. In Fig. 1C, corresponding to GO in air, the image profile shows that the variation of intensity is quite linear with the number of layers. Figure 1D presents a 3D image of GO flakes laid on the surface and imaged in water. The contrast enhancement offered by near-ARA layers allows us to easily distinguish monolayers from bilayers and few layers in different media (either air or water) and identify the number of layers at first sight. In addition, the technique permits an easy visualization of wrinkles, holes, and edge defects. Among the wide variety of 2D materials, GO is the most challenging to image because of its low absorption; however, the technique is not limited to graphene. Figure 1 (E and F) shows the images of MoS_2 and its assembly, with GO, into van der Waals heterostructures. Note that because of the better visibility of MoS_2, the dynamic range of the image is more important than for GO flakes alone; thus, the contrast of GO flakes in such mixed samples appears attenuated.

BALM is not specific to 2D nanomaterials, and every nanometer-thick material deposited on the ARA surface will appear with a very strong contrast because it will break the low reflectivity of the substrate. To illustrate this, we monitored the electrochemical deposition of copper on a BALM substrate by chronoamperometry, starting from a solution of $CuSO_4$ (10^{-2} M) at pH 2 (*31*). The schematic representation of the BALM-coupled electrochemical setup and the real-time visualization of copper deposition are given in fig. S1. This example, which is very different from 2D materials, illustrates the broadness of fields and applications covered by the technique. It also provides an example of the direct combination of BALM with another technique (here, electrochemistry).

To compare BALM with classical imaging techniques, we deposited the GO flakes on 5-nm Au near-ARA layers and imaged it using BALM, AFM, and SEM (fig. S2). BALM and AFM images show similar sensitivity to the presence of defects and wrinkles. Using AFM, the thickness of the GO flakes is estimated to be 1.3 nm; this value can be used to correlate the light intensity to the thickness and number of layers of GO. At that stage, the BALM technique already combines the information of AFM and the large scale and velocity of SEM with the simplicity and the cost of optical microscopy.

Taking advantage of the exceptional sensitivity of the technique, we show, hereafter, that it permits to observe tiny chemical modifications of GO. As a first example, we show how it can easily differentiate GO from r-GO. It is well established that GO can be reduced thermally or chemically to give r-GO (*32*). The removal of the oxygen species in GO results in a change of optical transmission (from transparent to slightly absorbing, up to 2.3% of the white light when approaching a complete reduction into graphene) and thickness (from ~1.5 to ~1.2 nm as it is typically measured by AFM). For this experiment, Cr (2 nm)/Au (5 nm) near-ARA layers were fabricated; chromium was first deposited on the glass substrate to improve the thermal and mechanical resistance of the gold film. Cr/Au near-ARA layers were first annealed in vacuum ($P = 5 \times 10^{-6}$ mbar) at 350°C for 6 hours, and then the GO flakes were deposited, reduced by thermal treatment (350°C for 1 hour), and imaged (Fig. 2A and fig. S3). Then, we deposited new GO flakes on the same surface and compared the images before and after this second deposition. Some regions show the superposition of r-GO and GO (Fig. 2, B and C, and fig. S3). The morphology of r-GO did not change compared to that of GO, indicating that the thermal reduction does not affect the integrity of the flakes. However, a large variation of reflected light intensity was observed. r-GO has a darker aspect than GO, as shown both in the images and the intensity profile in Fig. 2D. This observation is attributed to the difference of optical properties between r-GO and GO (*33*), although attenuated by the change of thickness, which has clearly an opposite effect (r-GO being thinner and darker than GO). The observed difference reveals that the technique is presently more sensitive to the refractive index than to the thickness, thus adding chemical sensitivity to the assets of the technique.

Numerical simulations based on the recursive Airy-Zernike formulae were performed using fixed values of *n* and *e* from the study by Jung *et al.* (*19*) for the refractive indices and thicknesses of GO and r-GO (see the Supplementary Materials for details). Figure S4 shows the contrast and intensity change of various stacks of GO and r-GO as a function of gold thickness. The reflectivity, averaged over angles from 0° to 30°, presents a minimum with respect to gold thickness. The Michelson contrast of one layer of GO on gold ARA is about 20% and shows a nearly linear variation with the number of layers. The simulations permitted to correctly

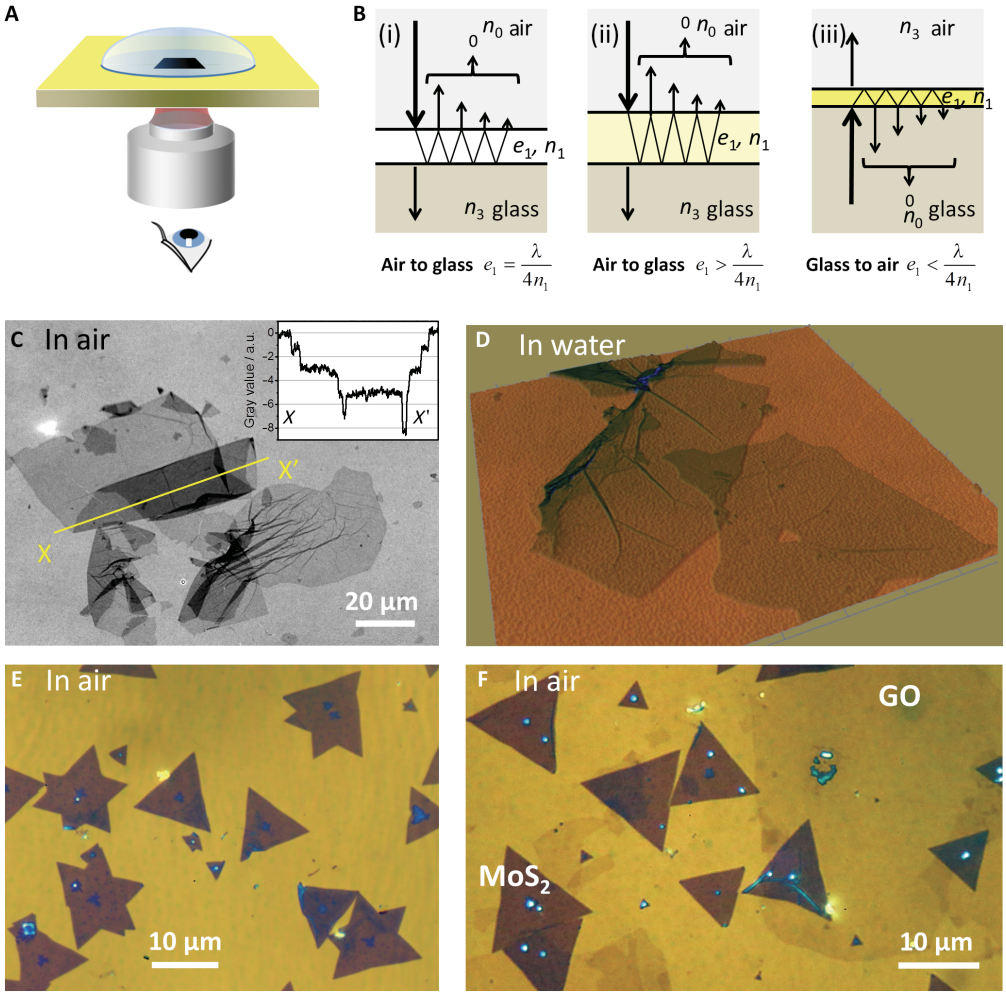

Fig. 1. Principle of BALM and example of images of 2D materials. (**A**) Representation of the BALM geometry: The image is obtained in reflected light microscopy; immersion oil avoids parasitic reflections between the objective and the transparent window. The near-ARA layer (here, a gold layer) is represented in yellow. The contrast is enhanced for the part of the sample that is very close to the surface and the half-space on the top remains accessible. (**B**) The AR property of a layer comes from the interferences between all reflected beams, as shown on the three schemes representing different situations for AR layers at the air/glass interface. From left to right: nonabsorbing AR layer (i), absorbing AR layer lighted from air (ii), and absorbing AR layer lighted from the glass (iii). In the first case (i), the AR condition is obtained for a layer of thickness of one-quarter of the wavelength (so-called quarter-wave layer). In the second case (ii), for the absorbing layer, it was previously shown that the layer must be thicker than quarter-wave (*36*–*38*); with highly absorbing materials, the absorption by the layer becomes so high that the light cannot reach the lower interface anymore and the destructive interferences are lost. In the third case (iii), by contrast, we demonstrate in the Supplementary Materials that the thickness of AR must be sub–quarter-wave and must become thinner as the layer material becomes more absorbing; the overall absorption of the layer remains low, and the light can always go through. Therefore, only the third configuration allows to make AR layers out of strongly absorbing materials. (**C**) BALM image of GO deposited on near-ARA and imaged in air (green channel, full contrast). Inset: Light intensity as a function of the number of layers. a.u., arbitrary units. (**D**) BALM image of GO obtained in water (RGB image with topographical representation of the total reflected intensity). (**E** and **F**) Images realized in air of MoS_2 and MoS_2 on GO; GO is still observable by transparency under the MoS_2 crystals. The purple structures on the MoS_2 triangles correspond to multilayers that start to grow on the monolayers.

reproduce the hierarchy of intensity observed in Figs. 1 and 2 for multilayers of GO and r-GO.

The previous experiments were static, thus not fully benefiting from the possibilities that offer a widefield optical imaging technique to study reactions in real time. We now turn to the functionalization of r-GO with oleic acid–coated Fe_3O_4 nanoparticles. Here, we were able to seamlessly visualize the 2D flakes before and after the adsorption of nanoparticles and again after desorption by rinsing with toluene (Fig. 3). To this end, 10 µl of Fe_3O_4 nanoparticles (with an average diameter of 5 nm) dispersed in toluene was deposited on the substrate. Immediately after the deposition of the drop, the objects were not visible because of the presence of the thin layer of the high-index solvent that strongly affects the images (fig. S5). After drying the surface, the r-GO flakes became observable again, and the presence of nanoparticles was observed. They accumulated and aggregated along the wrinkles of r-GO (Fig. 3B), because of either preferential absorption or evaporation. Numerical enlargement of the image in Fig. 3B, as displayed in Fig. 3D, suggests that the few nanoparticles seen in a defect-free part of the flake are individual particles that are observable despite their very small size. After washing with a drop of toluene and drying, the nanoparticles were removed (Fig. 3C and fig. S5). Although the solvent index in this experiment is not suited for in situ monitoring of adsorption/desorption kinetics, this example shows that BALM permits to probe local interactions between nanoparticles and r-GO flakes, which is of high importance for the development of new catalytic and energy conversion devices.

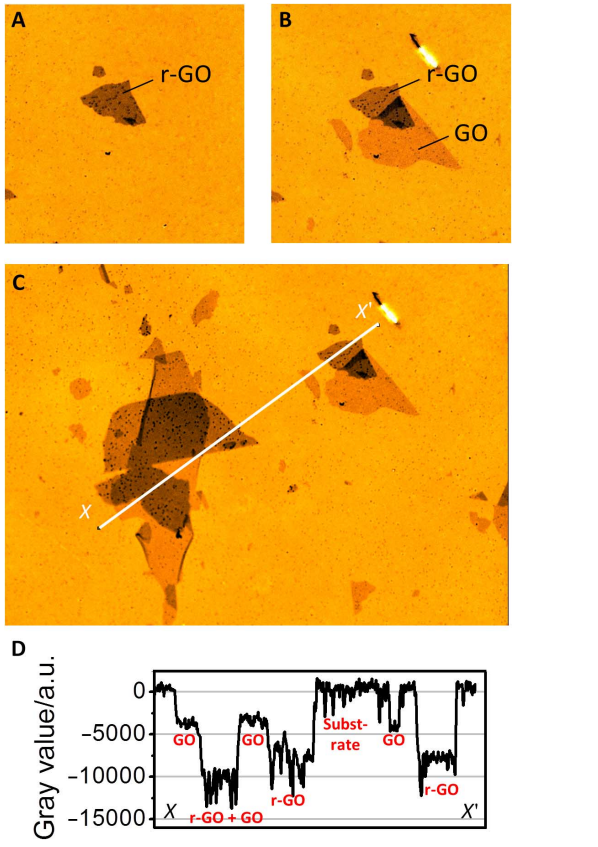

Fig. 2. Contrast between GO and r-GO. (**A**) BALM image of r-GO flakes. (**B** and **C**) BALM images (red channel) of r-GO flakes with GO deposited on top. (**D**) Light intensity profile showing GO and r-GO from (C).

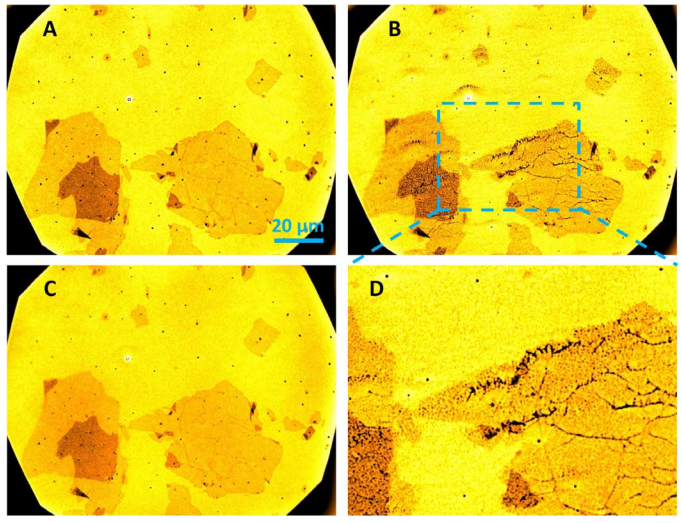

Fig. 3. Adsorption of Fe_3O_4 nanoparticles on r-GO. BALM images of r-GO (green channel and color scale "orange hot" of ImageJ software) flakes before (**A**) and after (**B**) the deposition of the 5-nm Fe_3O_4 nanoparticles. The particles tend to accumulate along the wrinkles of the r-GO flakes. (**C**) BALM image after rinsing the nanoparticles. (**D**) Enlargement of the area enclosed in blue rectangle in (B) showing the nanoparticle distribution along the wrinkles of r-GO.

Finally, we present an even more challenging experiment in which we monitored the adsorption of small organic molecules. GO flakes were deposited on a gold BALM substrate, and an area containing mono-, bi-, and trilayers, composed of folded and/or superposed GO flakes, was chosen. A drop of deionized water was deposited; the picture taken in pure water constitutes the reference of intensity. Then, a drop of positively charged pyrene [trimethyl-(2-oxo-2-pyrene-1-yl-ethyl)-ammonium bromide, M = 382.29 g mol^{-1}] (*34*) dissolved in water was added and we immediately started to record pictures (one every 6 s) to monitor the evolution of the light intensity induced by pyrene adsorption. The intensity was extracted from each image from the red channel on different areas of the gold surface and of the mono-, bi-, and trilayers (see Fig. 4E and fig. S6) and plotted as a function of time. Figure 4 (A to D) displays the intensity evolution extracted from 34 consecutive images taken within the first 5 min of the pyrene adsorption experiments for the four types of regions.

The intensity evolution is then fitted by a simple exponential decay function as follows: $Y_n^{(t)} = Y_n^{(0)} + A_n[1 - \exp(-t/\tau_n)]$, where τ_n is a characteristic time constant for n layers, $Y_n^{(0)}$ is the initial light intensity, and A_n is the total change in light intensity; the results of the fit are displayed in Fig. 4 (F to H). Figure 4F demonstrates the linear relationship between the intensity observed by BALM and the number of GO layers (as already seen in Fig. 1C). Figure 4G shows a similar dependence of the adsorption saturation level A_n with n. Such dependence demonstrates the adsorption and intercalation of pyrene on and in between the GO flakes. Figure 4H shows that such experiment allows extracting the characteristic time τ of the adsorption reaction. Although τ is ~77.1 s (±3.8) and 80.6 s (±5.0) for bi- and trilayer GO, it increases to 108.1 s (±8.2) for monolayers. For the bare gold substrate, the determination of τ is more sensitive to the fitting errors because the intensity evolution is much slower. Yet, the as-fitted value of 177.8 s (±35.7) is definitely much higher than for GO. We stipulate that because the pyrene derivative is positively charged, it adsorbs faster on the negatively charged GO flakes than on the neutral gold surface. The charges on monolayer GO would be intermediate because of the contact with the gold substrate. At a longer time scale, the intensity evolution cannot be fitted by a simple exponential decay function. The more complex dynamic is then probably due to the competition between adsorption and desorption time constants. The analysis of this regime requires further experiments and is beyond the scope of this study. At this stage, this experiment highlights the fact that the BALM technique allows the study of the dynamics of chemical reactions in a solvent, with full optical lateral resolution and sensitivity well below the molecular monolayer limit.

DISCUSSION

Here, we report a new high-resolution and very sensitive technique of microscopy called BALM, which is based on the use of AR layers made of absorbing materials. Only near-AR conditions (satisfying the thickness condition but not the index) were reached, but we already obtained an extreme sensitivity in the observation of various nanomaterials. As an example, BALM was used for imaging the reduction and the in situ functionalization of GO and r-GO. Besides the ability of BALM to visualize the 5-nm-diameter nanoparticles, we were able to follow the adsorption kinetics of a pyrene derivative on GO. This experiment also reveals the potential of BALM for the determination of affinity constants that will open new opportunities for sensing applications.

The technique is very simple to implement; it only requires the presence of an AR layer made of absorbing material and its lighting from the

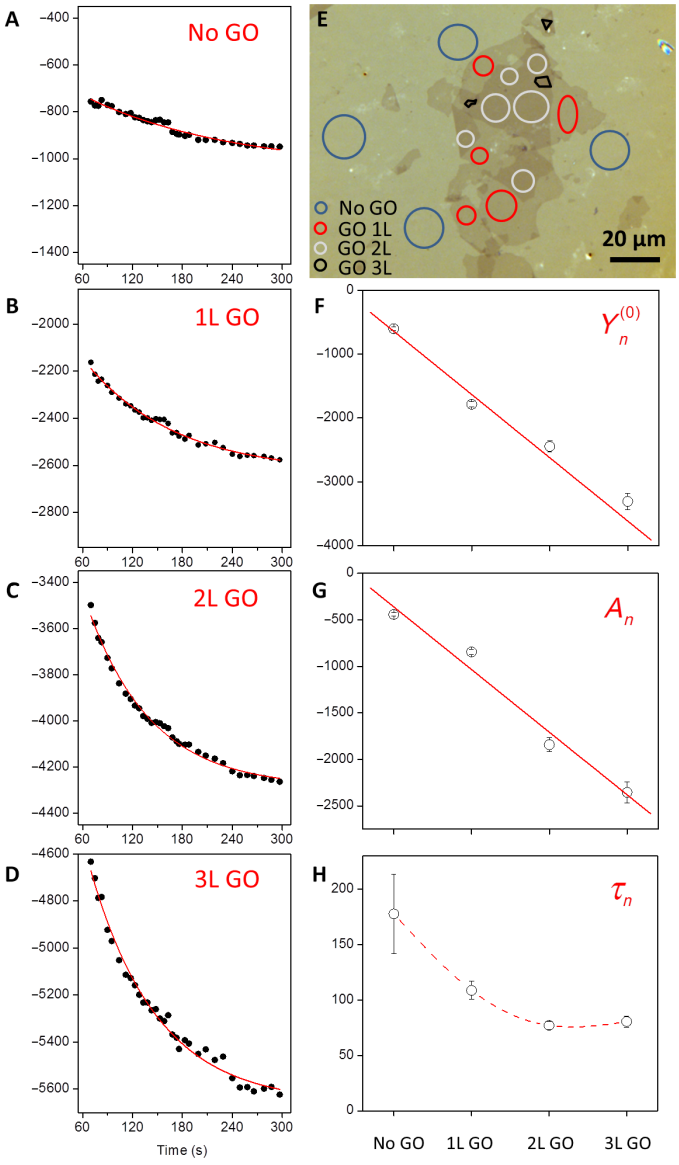

Fig. 4. Adsorption kinetics of a pyrene derivative on GO. (**A** to **D**) Evolution of intensity upon trimethyl-(2-oxo-2-pyrene-1-yl-ethyl)-ammonium bromide adsorption and intercalation [extracted from each image from the red channel on different areas of the gold surface and of the mono-, bi-, and trilayers as a function of time (black dots) and fit of the curves using an exponential decay function (red lines)]. (**E**) Raw RGB image of the GO flakes and areas used to extract the plotted data. (**F** to **H**) Plot of the fit parameters of the exponential decay function $Y_n^{(t)} = Y_n^{(0)} + A_n[1 - \exp(-t/\tau_n)]$. Red lines in (F) and (G) are linear fits.

high index medium (here, glass). The inverted microscope geometry makes the half-space (on top) accessible that permits to combine BALM with physical or chemical manipulation, or with other local probing techniques. Furthermore, ARA and near-ARA layers can be made of most conductive materials, allowing simultaneous electrical or electrochemical measurements. It was reported recently that absorbing ARCs (also called unconventional ARCs) have not yet found real applications because of the optical losses induced by the absorbing materials (*23*). The use of an extremely thin absorbing layer in backside configuration permits to overcome these limitations, and, finally, our work paves the way to the use of unconventional ARCs for a large range of applications from imaging to (bio)sensing.

MATERIALS AND METHODS

Graphite powder was purchased from Sinocarbon Materials Technology Co. GO was synthesized via the Hummers' method (*35*) and exfoliated following the procedure previously described (*30*). GO was deposited directly on the BALM substrate from the water solution or using the so-called bubble deposition method for samples imaged in air (*30*). Au (5 nm) and Cr/Au (2/5 nm) near-ARA layers were received from WATCH LIVE SAS (Lyon, France) or fabricated in the laboratory. Trimethyl-(2-oxo-2-pyrene-1-yl-ethyl)-ammonium bromide was prepared according to the procedure by Nakashima *et al.* (*34*). GO and r-GO were imaged using a Zeiss Axiovert 40 microscope equipped with a 63× Plan Apo oil immersion objective (numerical aperture of 1.40) and a Zeiss AxioCam HRc. AFM images were performed using a Dimension 3100 from Bruker (Digital Instruments); SEM images were performed using a Hitachi S4500 microscope. Chronoamperometry was carried out using a VoltaLab PGZ 301 potentiostat, in a three-electrode electrochemical cell developed for BALM under atmospheric conditions. The gold near-ARA layer was used as working electrode, a gold wire was used as counter electrode, and the Ag/AgCl electrode was used as the reference electrode.

SUPPPLEMENTARY MATERIALS

Supplementary material for this article is available at http://advances.sciencemag.org/cgi/content/full/3/5/e1601724/DC1

Demonstration of the formulae for antireflective layers made of absorbing materials

fig. S1. BALM-coupled electrochemical setup for real-time imaging of the electrochemical deposition of copper.

fig. S2. Comparison between BALM, AFM, and SEM images of GO.

fig. S3. Additional example of the difference of contrast between GO and r-GO.

fig. S4. Numerical simulations of contrast and intensity change of various stacks of GO/r-GO on an Au layer.

fig. S5. Images of the deposition and washing of nanoparticles on graphene.

fig. S6. Original image of the GO flakes used for pyrene adsorption experiments.

REFERENCES AND NOTES

1. F. Schwierz, Graphene transistors. *Nat. Nanotechnol.* **5**, 487–496 (2010).
2. K. S. Novoselov, V. I. Fal'ko, L. Colombo, P. R. Gellert, M. G. Schwab, K. Kim, A roadmap for graphene. *Nature* **490**, 192–200 (2012).
3. D. Jariwala, V. K. Sangwan, L. J. Lauhon, T. J. Marks, M. C. Hersam, Carbon nanomaterials for electronics, optoelectronics, photovoltaics, and sensing. *Chem. Soc. Rev.* **42**, 2824–2860 (2013).
4. W. Han, R. K. Kawakami, M. Gmitra, J. Fabian, Graphene spintronics. *Nat. Nanotechnol.* **9**, 794–807 (2014).
5. Z. Sun, A. Martinez, F. Wang, Optical modulators with 2D layered materials. *Nat. Photonics* **10**, 227–238 (2016).
6. K. S. Novoselov, A. Mishchenko, A. Carvalho, A. H. Castro Neto, 2D materials and van der Waals heterostructures. *Science* **353**, aac9439 (2016).
7. I. V. Lightcap, P. V. Kamat, Graphitic Design: Prospects of graphene-based nanocomposites for solar energy conversion, storage, and sensing. *Acc. Chem. Res.* **46**, 2235–2243 (2013).
8. D. Chen, H. Zhang, Y. Liu, J. Li, Graphene and its derivatives for the development of solar cells, photoelectrochemical, and photocatalytic applications. *Energy Environ. Sci.* **6**, 1362–1387 (2013).
9. C. Xu, B. Xu, Y. Gu, Z. Xiong, J. Sun, X. S. Zhao, Graphene-based electrodes for electrochemical energy storage. *Energy Environ. Sci.* **6**, 1388–1414 (2013).
10. F. Bonaccorso, L. Colombo, G. Yu, M. Stoller, V. Tozzini, A. C. Ferrari, R. S. Ruoff, V. Pellegrini, Graphene, related two-dimensional crystals, and hybrid systems for energy conversion and storage. *Science* **347**, 1246501 (2015).
11. D. Higgins, P. Zamani, A. Yu, Z. Chen, The application of graphene and its composites in oxygen reduction electrocatalysis: A perspective and review of recent progress. *Energy Environ. Sci.* **9**, 357–390 (2016).
12. S. Garaj, W. Hubbard, A. Reina, J. Kong, D. Branton, J. A. Golovchenko, Graphene as a subnanometre trans-electrode membrane. *Nature* **467**, 190–194 (2010).
13. C. Chung, Y.-K. Kim, D. Shin, S.-R. Ryoo, B. Hee Hong, D.-H. Min, Biomedical applications of graphene and graphene oxide. *Acc. Chem. Res.* **46**, 2211–2224 (2013).

14. Y. Liu, X. Dong, P. Chen, Biological and chemical sensors based on graphene materials. *Chem. Soc. Rev.* **41**, 2283–2307 (2012).
15. A. Bianco, Graphene: Safe or toxic? The two faces of the medal. *Angew. Chem. Int. Ed. Engl.* **52**, 4986–4997 (2013).
16. P. Blake, E. W. Hill, A. H. Castro Neto, K. S. Novoselov, D. Jiang, R. Yang, T. J. Booth, A. K. Geim, Making graphene visible. *Appl. Phys. Lett.* **91**, 063124 (2007).
17. S. Roddaro, P. Pingue, V. Piazza, V. Pellegrini, F. Beltram, The optical visibility of graphene: Interference colors of ultrathin graphite on SiO_2. *Nano Lett.* **7**, 2707–2710 (2007).
18. R. R. Nair, P. Blake, A. N. Grigorenko, K. S. Novoselov, T. J. Booth, T. Stauber, N. M. R. Peres, A. K. Geim, Fine structure constant defines visual transparency of graphene. *Science* **320**, 1308 (2008).
19. I. Jung, M. Pelton, R. Piner, D. A. Dikin, S. Stankovich, S. Watcharotone, M. Hausner, R. S. Ruoff, Simple approach for high-contrast optical imaging and characterization of graphene-based sheets. *Nano Lett.* **7**, 3569–3575 (2007).
20. T. Sandström, M. Stenberg, H. Nygren, Visual detection of organic monomolecular films by interference colors. *Appl. Opt.* **24**, 472–479 (1985).
21. M. A. Kats, R. Blanchard, P. Genevet, F. Capasso, Nanometre optical coatings based on strong interference effects in highly absorbing media. *Nat. Mater.* **12**, 20–24 (2013).
22. C. F. Guo, T. Sun, F. Cao, Q. Liu, Z. Ren, Metallic nanostructures for light trapping in energy-harvesting devices. *Light Sci. Appl.* **3**, e161 (2014).
23. M. K. Hedayati, M. Elbahri, Antireflective coatings: Conventional stacking layers and ultrathin plasmonic metasurfaces, a mini-review. *Materials* **9**, 497 (2016).
24. T. Oyama, H. Ohsaki, Y. Tachibana, Y. Hayashi, Y. Ono, N. Horie, A new layer system of anti-reflective coating for cathode ray tubes. *Thin Solid Films* **351**, 235–240 (1999).
25. F. F. Schlich, R. Spolenak, Strong interference in ultrathin semiconducting layers on a wide variety of substrate materials. *Appl. Phys. Lett.* **103**, 213112 (2013).
26. M. A. Kats, D. Sharma, J. Lin, P. Genevet, R. Blanchard, Z. Yang, M. M. Qazilbash, D. N. Basov, S. Ramanathan, F. Capasso, Ultra-thin perfect absorber employing a tunable phase change material. *Appl. Phys. Lett.* **101**, 221101 (2012).
27. H. Dotan, O. Kfir, E. Sharlin, O. Blank, M. Gross, I. Dumchin, G. Ankonina, A. Rothschild, Resonant light trapping in ultrathin films for water splitting. *Nat. Mater.* **12**, 158–164 (2013).
28. J. Park, J.-H. Kang, A. P. Vasudev, D. T. Schoen, H. Kim, E. Hasman, M. L. Brongersma, Omnidirectional near-unity absorption in an ultrathin planar semiconductor layer on a metal substrate. *ACS Photonics* **1**, 812–821 (2014).
29. D. Ausserré, R. Abou Khachfe, L. Roussille, G. Brotons, L. Vonna, F. Lemarchand, M. Zerrad, C. Amra, Anti-reflecting absorbing layers for electrochemical and biophotonic applications. *J. Nanomed. Nanotechnol.* **5**, 1000214 (2014).
30. J. Azevedo, S. Campidelli, D. He, R. Cornut, M. Bertucchi, S. Sorgues, J. J. Benattar, C. Colbeau-Justin, V. Derycke, Versatile wafer-scale technique for the formation of ultrasmooth and thickness-controlled graphene oxide films based on very large flakes. *ACS Appl. Mater. Interfaces* **7**, 21270–21277 (2015).
31. D. Grujicic, B. Pesic, Electrodeposition of copper: The nucleation mechanisms. *Electrochim. Acta* **47**, 2901–2912 (2002).
32. C. K. Chua, M. Pumera, Chemical reduction of graphene oxide: A synthetic chemistry viewpoint. *Chem. Soc. Rev.* **43**, 291–312 (2014).
33. J. Kim, F. Kim, J. Huang, Seeing graphene-based sheets. *Mater. Today* **13**, 28–38 (2010).
34. N. Nakashima, Y. Tomonari, H. Murakami, Water-soluble single-walled carbon nanotubes via noncovalent sidewall-functionalization with a pyrene-carrying ammonium ion. *Chem. Lett.* **31**, 638–639 (2002).
35. W. S. Hummers Jr., R. E. Offeman, Preparation of graphitic oxide. *J. Am. Chem. Soc.* **80**, 1339 (1958).
36. M. Born, E. Wolf, *Principles of Optics* (Pergamon Press, ed. 6, 1980).
37. R. M. A. Azzam, N. M. Bashara, *Ellipsometry and Polarized Light* (North-Holland, 1987).
38. S. G. Moiseev, S. V. Vinogradov, Design of antireflection composite coating based on metal nanoparticles. *Phys. Wave Phenom.* **19**, 47–51 (2011).

Acknowledgments: We thank WATCH LIVE SAS for helping us to become first users of the BALM technique. **Funding:** This work was supported by a public grant overseen by the French National Research Agency (ANR) as part of the "Investissements d'Avenir" program (Laboratory of Excellence NanoSaclay, reference no. ANR-10-LABX-0035).
Author contributions: D.A. invented the technique. S.C., K.J., J.M., R.C., V.D., and D.A. performed the experiments and analyzed the data. D.A. established the optical equations with the help of C.A., R.A.K., and M.Z. R.A.K. and M.Z. checked all the results with two independent numerical approaches (Airy recursive and Matrix methods). C.A. realized and characterized the ultrathin contrast layers. S.C. supervised the redaction of the manuscript with the help of V.D. and D.A. **Competing interests:** The authors declare that they have no competing interests. Institutional review board and/or Institutional Animal Care and Use Committee guidelines are not applicable for this work. **Data and materials availability:** All data needed to evaluate the conclusions in the paper are present in the paper and/or the Supplementary Materials. Additional data are available from and requests for materials should be addressed to S.C. (stephane.campidelli@cea.fr) or to D.A. (dominique.ausserre@univ-lemans.fr).

Submitted 25 July 2016
Accepted 10 March 2017
Published 12 May 2017
10.1126/sciadv.1601724

Citation: S. Campidelli, R. Abou Khachfe, K. Jaouen, J. Monteiller, C. Amra, M. Zerrad, R. Cornut, V. Derycke, D. Ausserré, Backside absorbing layer microscopy: Watching graphene chemistry. *Sci. Adv.* **3**, e1601724 (2017).